Applied Materials Today 20 (2020) 100709

Contents lists available at ScienceDirect

Applied Materials Today

journal homepage: www.elsevier.com/locate/apmt

# Enhancing the nanoplasmonic signal by a nanoparticle sandwiching strategy to detect viruses

Fatih Inci[a,f], Merve Goksin Karaaslan[a], Amideddin Mataji-Kojouri[a], Pir Ahmad Shah[b], Yeşeren Saylan[a,c], Yitian Zeng[d], Anirudh Avadhani[a], Robert Sinclair[d], Daryl T.-Y. Lau[b,*], Utkan Demirci[a,e,*]

[a] Bio-Acoustic MEMS in Medicine (BAMM) Laboratory, Canary Center at Stanford for Cancer Early Detection, Department of Radiology, Stanford School of Medicine, Stanford University, Palo Alto, CA, 94304, USA
[b] Liver Center, Department of Medicine, Beth Israel Deaconess Medical Center, Harvard Medical School, Boston, MA, 02115, USA
[c] Department of Chemistry, Hacettepe University, Ankara 06800, Turkey
[d] Department of Materials Science and Engineering, Stanford University, Stanford, CA, 94304, USA
[e] Department of Electrical Engineering (by courtesy), Stanford University, Stanford, CA, 94305, USA
[f] UNAM - Institute of Materials Science and Nanotechnology, Bilkent University, Ankara 06800, Turkey

ARTICLE INFO

*Article history:*
Received 24 December 2019
Revised 25 April 2020
Accepted 20 May 2020

*Keywords:*
Nanoparticles
Nanoplasmonics
Sandwich assays
HBV diagnosis
High-throughput assays

ABSTRACT

Nanoparticles that can assemble and bind selectively on surfaces in intricate geometries can trigger multiple plasmonic modalities and enable wide applications in agriculture such as pesticide monitoring, in medical imaging such as targeted cancer detection, in bioengineering such as biotarget detection and biosensing, and in healthcare such as selection of drugs and their binding kinetics. However, these particles mainly rely on binding of the target to a surface to create a plasmonic resonance and subsequent shifts by binding of biotargets, which limit the flexibility to control overall sensitivity. Here, we present an unconventional way that sandwiches a virus (*i.e.,* Hepatitis B virus: HBV) topographically between two or more nanoparticles on the top and the bottom to create a double-step shifting effect amplifying the total resonance wavelength shift on the surface by 1.53 - 1.77 times that significantly enhances the sensitivity. We successfully applied this approach to an intact HBV sensing application, which accurately quantified the viral load. This method establishes a new nanoparticle-based sandwiched nanoplasmonic approach to detect and quantify viral load using two-step sensing with broad applications in biosensing.


## 1. Introduction

Nanoparticles have enabled sensing of nanoscale biotargets such as proteins, lipids, and viruses [1]. The size scale of nanoparticles aligns well with the scale of biological entities that are of interest for many medical and bioengineering applications [2]. Although the scale is matching, the detection of binding events in nanoscale only lead to small perturbations on the resonance leading to smaller detectible signals [3,4]. This especially becomes an insurmountable task for detecting viruses that can be very rare in numbers in solutions [4]. Hence, alternative methods that can enhance and amplify the perturbations in the resonance and allow larger shifts that are visible and quantifiable are urgently needed to advance the field.

Over the years, advances in optics and nanoparticle measurement techniques allow very sensitive imaging tools to be created [5,6]. For instance, photonic crystals can allow imaging of single nanoparticles bound to the surfaces using stages precise down to a fraction of a nanometer and high-end optical lenses leading to extremely precise configurations that can only operate on vibration-free setups [7]. These tools can scan a smaller surface in hours to detect a measurable signal mapping the surface, however, their utility beyond specialized lab settings limits their application and affordability for broad availability for labs or end-users in the healthcare industry [8].

Inexpensive, widely-available, rapid, and sensitive virus detection tools that can be deployed at once surveying multiple sites, are critical to prevent, monitor' and manage epidemics and biothreats. For instance, worldwide, infectious diseases are the lead-

* Corresponding authors.
*E-mail addresses:* utkan@stanford.edu (U. Demirci), dlau@bidmc.harvard.edu (D. T.-Y. Lau).

https://doi.org/10.1016/j.apmt.2020.100709
2352-9407/

ing causes of death, and pose significant burden on global health [9–11]. The prevalence of cancer is particularly high in developing countries, where infectious diseases are also common [12–16]. Even in the United States, liver cancer incidence has increased more than three times since 1980 [17] whereas it has higher mortality in developing countries, where ~80% of the burden occurs [18]. Globally, hepatitis B virus (HBV) is the most common cause of primary hepatocellular carcinoma (HCC)–the most common form of liver cancer [16–19]. It is, therefore, important to develop technologies that can detect oncogenic viruses, especially HBV, among at-risk patient populations in developing countries that would facilitate antiviral treatment and HCC surveillance to minimize cancer mortality.

Currently, diagnosing virus-induced cancer is largely based on the detection and quantification of the viral nucleic acids (*i.e.,* RNA or DNA), elevated HCC secreting protein levels (*i.e.,* alpha-fetoprotein (AFP)) or liver imaging. HBV viral load is the most important independent predictor of HCC risk. The land-mark natural history study from Taiwan [19] reported incremental HCC rates with HBV DNA levels increased over 2,000 IU/mL ($10^{3.3}$ IU/mL) even after controlling for other host and viral factors. Besides assessing the risk for HCC, quantifying the replicative levels of HBV is critical for the initiation of antiviral therapy and monitoring of treatment response. While quantitative PCR assays are routinely available in developed countries [20], it is difficult to implement them in developing regions of the world due to high costs, limited infrastructure, high maintenance costs, and the need for skilled personnel. Further, enzyme-linked absorption assay (ELISA) is used to detect protein biomarkers to screen HCC and to monitor tumor progression. While these nucleic acid and protein biomarker-based technologies have been validated using expensive infrastructure [21–23], translating these methods for rapid point-of-care (POC) testing at resource-limited settings has been extremely challenging [19,24]. Therefore, the World Health Organization (WHO) emphasizes the urgent need to develop inexpensive, disposable, easy-to-use devices for resource-constrained settings. There are, however, no diagnostic and screening assays available that can detect oncoviruses in a simple, rapid, and inexpensive manner at the POC settings.

Recent advances in the nanotechnology and sensors have enabled to develop new strategies for detecting either viral DNA, proteins, or serological content through electrical, mechanical, and optical sensors [8]. In particular, considering assay cost and ease-of-use parameters, electrochemical sensors have been integrated with paper substrates for detection of HBV DNA [7]. However, ionic content of biological fluids has been challenging for their detection accuracy. Although some of electrochemical sensor designs with an improved sensitivity, integrating graphene quantum dots and gold (AuNP)-embedded polyaniline nanowires [25], have been tested with biological matrices, their multi-step fabrication and the need for sophisticated tools are still considerable bottlenecks for their implementation to the POC settings. Sandwich ELISA as a sensing concept has been developed and widely used in a variety of multi-modal sensing applications in proteins and cells [26]. Despite the notable improvements in the conventional ELISA sensitivity, lengthy assay time (>5 hours) and labor-intensive manipulations (washing steps) are still challenging their deployment to the POC settings [26]. In optical sensor realm, others have taken this sandwich-ELISA approach and tested it for photonic crystals in protein sensing [7,27]. Further, biosensing through plasmonically-active surface traditionally rely on the binding of the target to a surface as represented in our work [28–31] and the work by others [32–38]. Plasmonic or nanoparticle-based detection has also been adapted to the sandwich-ELISA strategy. For instance, a microchip was developed to detect HIV antigen proteins through a chemical reaction (*i.e.,* the growth of metal layer with silver ions) with antibody-AuNP conjugates [39]. Moreover, a nanofabricated plasmonic chip was applied to detect nano-sized cellular entities, *i.e.,* exosomes, and their signal levels were enhanced by attaching nanostar-shaped AuNPs to the captured exosomes [40], and then, further improvements with dark-field imaging strategy reached to detect a single exosome with AuNP-tagging [41], yet limiting their use in highly sophisticated optical sensing laboratories only. Consequently, these nanotechnological advances have only improved one or two facets from the detection perspective, however, some critical challenges remained unaddressed for a POC testing at resource-limited settings that were outlined by the WHO's ASSURED criteria (Affordable, Sensitive, Specific, User-friendly, Rapid and robust, Equipment-free, Deliverable)-a benchmark for POC platforms tests to evaluate their potential for healthcare facilities in rural and resource-limited settings [42,43]. Therefore, unaffordable assay cost, labor-intensive nanolithography-based fabrication, lengthy experimental steps/assay time, the need for sophisticated equipment/facilities, skilled personnel, and external reactions for signal enhancements (*e.g.,* silver-gold growth after the antibody-AuNP label) are remaining challenges for the adaptation of existing sensor systems at the POC for resource-limited settings.

To address some of these challenges, we earlier demonstrated a nanoplasmonic-based technology for potential clinical applications [30], as well as a proof-of-principle study focusing on the detection of HBV from biological samples *via* collecting wavelength spectra of AuNPs on the sensor surface upon the capture of viruses [29]. Although a specific body of proof-of-concept work exists, the sensing mechanism is based on direct binding of viruses to a surface only leading to a small range wavelength shift. Here, we demonstrate a new approach by sandwiching of a virus between a plasmonic layer of AuNPs and a secondary layer of AuNPs (Fig. 1). Further, there has been minimal assessment on the optimization of surfaces and understanding the sensing mechanisms with theoretical analysis. Here, we take the concept of sandwiching a molecule from ELISA and translate this concept to sandwiching a virus between two or more gold nanoparticles and a nanoparticle surface to create a large plasmonic sensing effect on the sensor surface. This 'doubling down strategy19; amplifies the nanoplasmonic response in biosensing, hence increasing the detected signal intensity and associated sensitivity. In this study, we show major progress on the fabrication and extensive characterization of the nanoplasmonic platform, including experimental analyses and theoretical simulations, for HBV viral load measurements. Briefly, the fabrication is simplified into a two-step procedure: (i) immobilizing poly-L-lysine (PLL) residues on a 96-well plate, and (ii) creating both nanoplasmonic and sensing layer *via* anti-HBV surface antibody-coated AuNP complexes (Ab-AuNP). With numerical assessments, we have comprehensively analyzed the distance between Ab-AuNPs to create efficient detection performance. In addition, the presented platform has dual-detection capability: (i) direct detection (label-free sensing) of intact HBV, and (ii) amplified nanoplasmonic detection (labeled sensing with a secondary Ab-AuNP) of intact HBV. In addition to these technical highlights, considering the ASSURED criteria, the presented platform in a 96-well format can be easily integrated with current laboratory procedures and existing lab equipment (*e.g.,* a pipette and standard spectrometric plate reader) that can be readily available in a standard laboratory. This broadens the usability of assay without the need for skilled personnel, as well as potentially enables highly scalability and high-throughput. In addition, short assay time (1 hour) and affordable material/reagents (costing at <$2 per well/assay) highlight our platform's potential that with further development it can be adapted as a POC test at the resource-scarce settings.

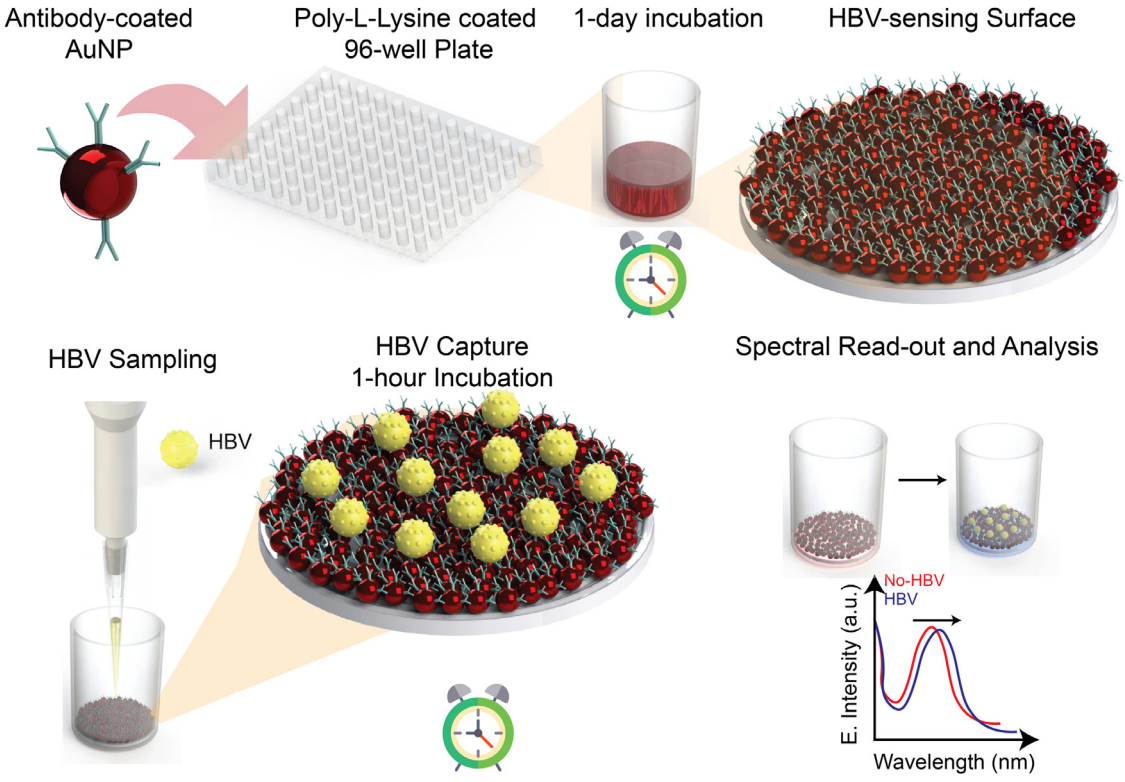


**Fig. 1.** Schematic of workflow in HBV detection assay. Briefly, anti-HBV surface (HBs), Antigen (Ag) antibody-coated gold nanoparticles are applied into a 96-well plate, which is decorated with poly-L-lysine molecules on the surface. After one-day incubation, HBV sensing area is formed on the well plate and measured using a standard plate reader. HBV samples are then directly applied to the surfaces and incubated for an hour at room temperature. After washing the unbound virus particles and impurities, the sensing surface is measured again. The results are plotted to evaluate the binding of HBV.

## 2. Results and discussions

### *2.1. Evaluating surface chemistry and fabrication of nanoplasmonic sensor*

The nanoplasmonic surface is fabricated with two main layers: (i) PLL as an adhesive layer to connect the nanoplasmonic sensing layer to polystyrene well surface, and (ii) Ab-AuNPs as a sensing layer. In this regard, we initially designed an experimental set evaluating the concentrations of PLL in terms of peak wavelength and extinction intensity values (Fig. 2A-B). The concentration of Ab-AuNP stock solution was $\sim 8 \times 10^{12}$ particles/mL as stated by the manufacturer. In this study, the stock solution was serially diluted with phosphate buffered saline (PBS) to adjust the concentrations used in the optimization steps. We tested 0.05 – 1 mg/mL of PLL concentrations when $2 \times 10^{12}$ Ab-AuNPs/mL was applied to the PLL-coated surfaces and incubated for 18 hours. Wavelength spectra showed increments proportional to the PLL concentrations, resulting in peak wavelength values from 530.1 ± 0.4 nm to 541.2 ± 1.8 nm that indicates the formation of more binding sites for Ab-AuNP immobilization. In particular, 0.5 to 1.0 mg/mL of PLL concentrations provided statistically comparable peak wavelength and extinction intensity values ($n$=3-4, $p$>0.05). Further, 0.75 mg/mL of PLL resulted in a high extinction intensity value, pointing that the number of amine groups has a critical role in transition from donating binding sites to collapsed polymer form on the substrate [44]. We, therefore, continued the experiments with 0.75 mg/mL concentration of PLL.

Similarly, different Ab-AuNP concentrations ($8 \times 10^{10}$ to $8 \times 10^{12}$ Ab-AuNPs/mL) were evaluated while keeping PLL concentration (0.75 mg/mL) and Ab-AuNP incubation time (18 hours) constant (Fig. 2C-D). We observed the binding of Ab-AuNP at lower concentrations ($8 \times 10^{10}$ to $32 \times 10^{10}$ Ab-AuNPs/mL), but these concentrations did not provide a significant peak in the curve and they resulted in lower peak wavelength values due to the lesser number of Ab-AuNP on the well surface. The peak wavelength values were reported as 537 ± 0.1 nm for $8 \times 10^{10}$ and $16 \times 10^{10}$ Ab-AuNPs/mL concentrations, and 537.8 ± 1.1 nm for 4% of Ab-AuNP. When increasing concentrations of Ab-AuNP, we observed the formation of a clear peak curve starting from $8 \times 10^{11}$ Ab-AuNPs/mL concentration, and the curve provided sharper peaks at higher concentrations of Ab-AuNP ($4 \times 10^{12}$ and $8 \times 10^{12}$ Ab-AuNPs/mL concentrations). In particular, $4 \times 10^{12}$ Ab-AuNPs/mL concentration provided better characteristics in terms of wavelength spectra compared to the stock solution ($8 \times 10^{12}$ Ab-AuNPs/mL), but the peak wavelength and extinction intensity values for these two Ab-AuNP concentrations were statistically similar ($n$=4, $p$>0.05). In the following experiments, we used $4 \times 10^{12}$ Ab-AuNPs/mL concentration for forming the nanoplasmonic layer.

In addition to the surface chemistry parameters, we also assessed the effect of Ab-AuNP incubation time over the sensor formation (Fig. 2E-F). In this regard, we tested a broad range of incubation time spanning from 30 minutes to 24 hours when the surfaces were prepared with optimized PLL and Ab-AuNP concentrations stated above. As shown in Fig. 2E, the formation of nanoplasmonic layer started from 30 minutes and 1 hour of incubation, which had a lower amplitude of wavelength spectra compared to the other time slots. Stable and higher amplitude of wavelength spectra started from 3 hours of incubation and reached the highest extinction intensity level at 24 hours of incubation. The heat-map plot clearly indicates the changes in extinction intensity spectra as a function of incubation time (Fig. 2F). According to these observations, we chose a 24-hour incubation time for Ab-AuNP immobilization for further experiments.

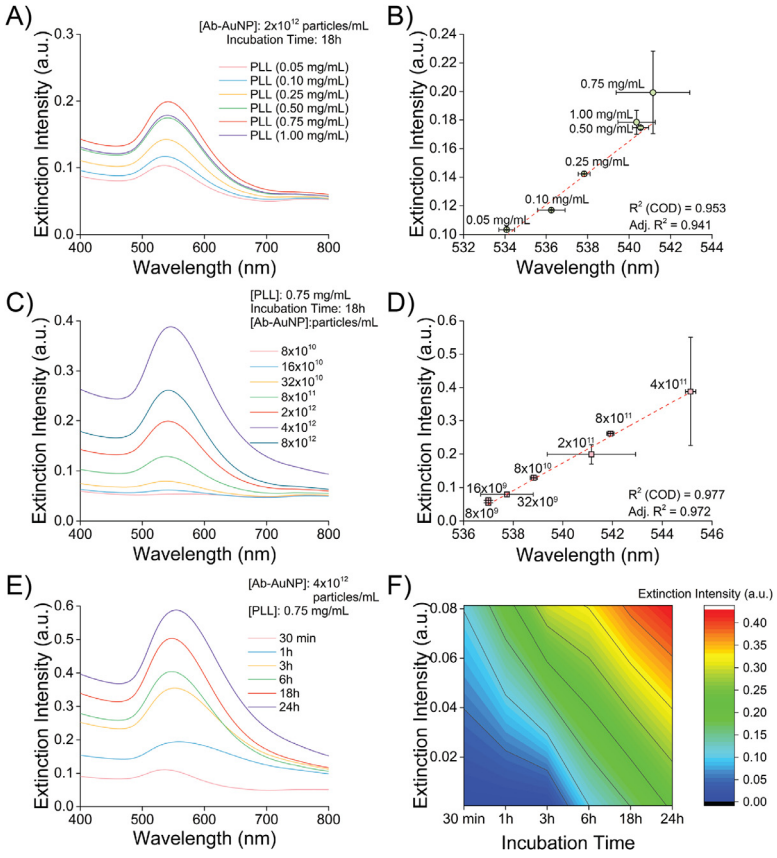


**Fig. 2.** Evaluation of surface chemistry steps and incubation time. The sensing area was created with two different layers: poly-L-lysine (PLL) and antibody-coated AuNP (Ab-AuNP). A) Various concentrations of PLL ranging from 0.05 to 1 mg/mL were evaluated when $2 \times 10^{12}$ particles/mL concentration of Ab-AuNP and 18 hours of incubation time were applied. B) Depending on increments of PLL concentration, the extinction intensity values increased. This value decreased at the concentration of 1 mg/mL, indicating steric hindrance occurred at the highest PLL concentration. In addition, 0.5 to 1.0 mg/mL of PLL concentrations resulted in statistically comparable peak wavelength and extinction intensity values ($n$=3-4, $p$>0.05). Since 0.75 mg/mL of PLL provided a high extinction intensity value, we therefore continued the experiments with 0.75 mg/mL concentration of PLL. C) Different concentrations ranging from $8 \times 10^{10}$ to $8 \times 10^{12}$ Ab-AuNPs/mL were evaluated when PLL concentration and incubation time were 0.75 mg/mL and 18 hours, respectively. D) Depending on increments of Ab-AuNP concentration, the extinction intensity values increased. Similarly, at the highest concentration of Ab-AuNP ($8 \times 10^{12}$ Ab-AuNPs/mL), we observed a decrease in the extinction intensity value, indicating a potential steric hindrance. At the $4 \times 10^{12}$ Ab-AuNPs/mL concentration, we observed better characteristics in terms of wavelength spectra compared to the stock solution ($8 \times 10^{12}$ Ab-AuNPs/mL), but the peak wavelength and extinction intensity values for these two concentrations were statistically comparable ($n$=4, $p$>0.05). We therefore used $4 \times 10^{12}$ Ab-AuNPs/mL concentration to create the nanoplasmonic layer. E) Accordingly, we continued the optimized surface chemistry step parameters (Ab-AuNP: $4 \times 10^{12}$ Ab-AuNPs/mL and PLL: 0.75 mg/mL), and evaluated the incubation time in terms of extinction intensity and wavelength peak values. F) Heat-map plot depicted that the incubation time improved the immobilization of Ab-AuNP and the highest extinction intensity value was reached at 24-hour incubation.

### 2.2. Characterizing the nanoplasmonic platform

Initially, we analyzed the size distribution of Ab-AuNPs *via* transmission electron microscopy (TEM) and observed monodispersed characteristics of particles with a mean diameter of about 30 nm (Fig. 3A). We then measured the optical absorbance measurements of these conjugates, and observed the peak wavelength at ~530 nm (Fig. S1). Following the PLL immobilization, Ab-AuNPs were decorated on the well surface, and the final surface was confirmed with multiple surface characterization methods. With contact angle measurements, we evaluated hydrophilicity properties of the bare and nanoplasmonic surfaces. The contact angle value of the well surface altered from 65.9° ± 2.7 to 42.5° ± 7.7, indicating that the immobilization of Ab-AuNPs generated more hydrophilic surface (Fig. 3B). We then performed Atomic Force Microscopy (AFM) to evaluate the roughness parameter (after Ab-AuNP immobilization) (Fig. 3C). The height variations of the nanoplasmonic surface were examined along the hypotenuse of each scanned image (1 $\mu$m x 1 $\mu$m), resulting in ~0.68 nm of roughness (RMS: Root mean square). This information indicated a smooth distribution of Ab-AuNPs on the well surface. To confirm chemical characteristics of sensor surface, we performed Attenuated Total Reflectance Fourier-Transform Infrared Spectroscopy (ATR-FTIR) measurements, spanning from 500 to 3750 $cm^{-1}$ of wavenumbers (Fig. 3D). The IR spectra of bare polystyrene was subtracted from that of nanoplasmonic surface. As a result, the IR peaks appearing at 1646 $cm^{-1}$, 1492 $cm^{-1}$ and 1446 $cm^{-1}$ were observed due to the C=O stretching, aromatic C=C stretching, and C-N bending bands. There were also N-H bending bands overlapped at this region in the spectrum. The sharp peaks appearing between 600-744 $cm^{-1}$ corresponded to the C-H (aromatic) out of plane stretching bands. The narrow peak appearing at 3363 $cm^{-1}$ overlapped with the stretching bands of both N-H group (3100-3500 $cm^{-1}$) and aromatic C-H groups (3050-3150 $cm^{-1}$). All these characterization methods including size measurements, hydrophilicity, nanoscale imaging, and chemical modifications, pointed the successful modifications on the well surface.

### 2.3. Numerical simulations for nanoplasmonic signal

During the preparation of the nanoplasmonic substrate, the Ab-AuNPs self-assembled on the PLL-coated surface, and therefore, the inter-particle spacing in our experiments was determined by two factors: (i) the Ab-AuNP concentration in the solution, and (ii) the

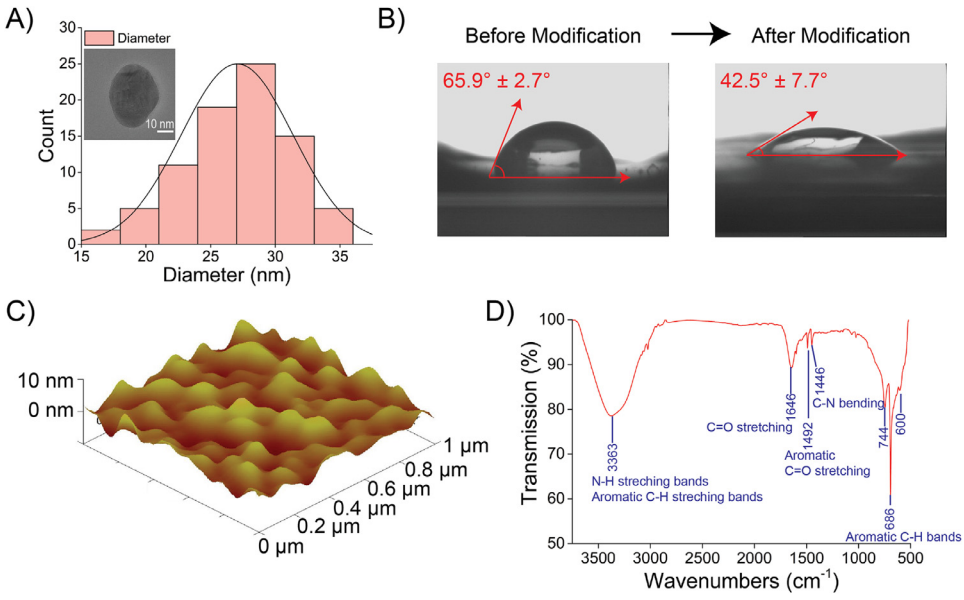


**Fig. 3.** Characterization of the sensing surface. A) Anti-HBV surface (HBs), Antigen (Ag) antibody-coated AuNP (Ab-AuNP) molecules were characterized using Transmission Electron Microscopy (TEM). The size of particles was around 30 nm and they were mostly uniform in size. B) We next immobilized the Ab-AuNP to the poly-L-lysine (PLL) coated well plate. Before and after modification of the well plate was imaged and the contact angle of these surfaces were evaluated. The bare surface provided more hydrophobic characteristics (65.9° ± 2.7°), whereas the modified surface was more hydrophilic (42.5° ± 7.7°) after the immobilization of PLL and Ab-AuNP. C) The HBV-sensing surface was imaged using Atomic Force Microscopy (AFM). The surface was scanned 1 × 1 µm D) The Fourier-transform infrared spectroscopy (FTIR) spectra of sensing surface was recorded at room temperature in the range 3750–500 $cm^{-1}$. The peaks due to the chemical vibrations were demonstrated in the plot.

PLL concentration on the surface. We evaluated the changes in the resonance wavelength and the magnitude of extinction intensity by increasing the concentration of either PLL or Ab-AuNPs in our experiments. As shown in Fig. 2, we observed an increase in the magnitude of extinction intensity and a red-shift in the resonance wavelength. Our simulations also revealed that this could be related to an increase in the surface concentration of Ab-AuNPs, eventually resulting in a smaller inter-particle separation. In the simulations, we designed a lattice-format of Ab-AuNP organization on the PLL-coated surface (Figs. S2-S6). We considered the effect of both inter-particlar spacing (separation distance: S) for Ab-AuNPs (with a Diameter: D) on the resonance wavelength (Fig. 4A). We then calculated the extinction spectra of an Ab-AuNP on the PLL-coated surface for different ratios of inter-particle spacing to particle diameter (S/D) ranging from 1.05 to 3 (Fig. 4B). As a result, a lower inter-particle spacing leads to both higher extinction intensity and red-shift in the resonance wavelength (Fig. 4C). By comparing simulation results (S/D = 1.05 to 1.4) with the measured extinction spectrum, we observed that the optimized conditions for Ab-AuNP and PLL concentrations produced the smallest inter-particle spacing. For instance, higher concentrations of Ab-AuNP at the optimized PLL concentration (0.75 mg/mL) indicate the lower inter-particle spacing as observed in the numerical calculations. These concentrations resulted in higher extinction intensity and red-shift in the resonance wavelength (Fig. 4D). In our AFM measurements (Fig. 3) of the optimized surface conditions, we observed an almost smooth surface, which could be attributed to a surface well-packed with nanoparticles. In addition, our recorded extinction spectra from different samples showed that we obtained a high extinction amplitude and a longer resonance wavelength for the optimized surface (Fig. 2C). This relationship was completely in line with our numerical calculations as well. An imaging system with a high resolution could be used to analyze the spacing between two adjacent particles for further investigations. In addition, we calculated electric-field distribution for this lattice-configuration (S/D = 1.4) at the resonance wavelength (Fig. 4E), which shows localized field enhancement around the nanoparticles when they are illuminated by an x-polarized plane wave.

### 2.4. Measuring HBV viral load

To evaluate the binding of HBV, we fabricated nanoplasmonic surfaces with the optimized procedure, and applied HBV samples isolated from patient sera (Fig. 5A). Initially, we compared the simulated and experimental data before and after HBV binding. Linewidths of the resonances for measurement curves were wider due to potential non-uniformity of Ab-AuNPs' size and different values of inter-particle gaps on different spots on the surface. In the simulation, considering the value of *S/D* ratio, HBVs were able to penetrate into the inter-particle gap of the adjacent Ab-AuNP and they simultaneously reacted with multiple nanoparticles. In simulation, there was a 1.8 nm resonance shift, and for the measurement case, it was 2.5 nm shift after the HBVs are captured (Fig. 5B).

We then designed an experimental set to evaluate HBV samples with different concentrations ranging from 10 to $10^5$ IU/mL, which were prepared by diluting the stock HBV Genotype C serum sample with PBS (Fig. 5C). This viral dynamic range was chosen based on clinical indications. Treatment guideline from the American Association for the Study of Liver Diseases (AASLD) recommended initiation of antiviral therapy for patients with chronic hepatitis B if their HBV DNA levels are persistently over 2,000 IU/mL ($10^{3.3}$ IU/mL) [45]. The available, commonly used standard-of-care assay has a detection limit of 10 IU/mL (m2000 Real-time HBV Assay, Abbott Diagnostics). This low level of detection is essential to monitor antiviral treatment response.

All measurements including before and after the HBV exposure were performed under PBS condition. The plate was also washed with PBS after the virus exposure. Accordingly, we subtracted the data (peak wavelength point) before and after the HBV exposure under PBS conditions to avoid any refractive index changes associated with the measurements. In addition, the control was defined as 1:1000 (v:v) dilution of serum samples in PBS. This dilution rate

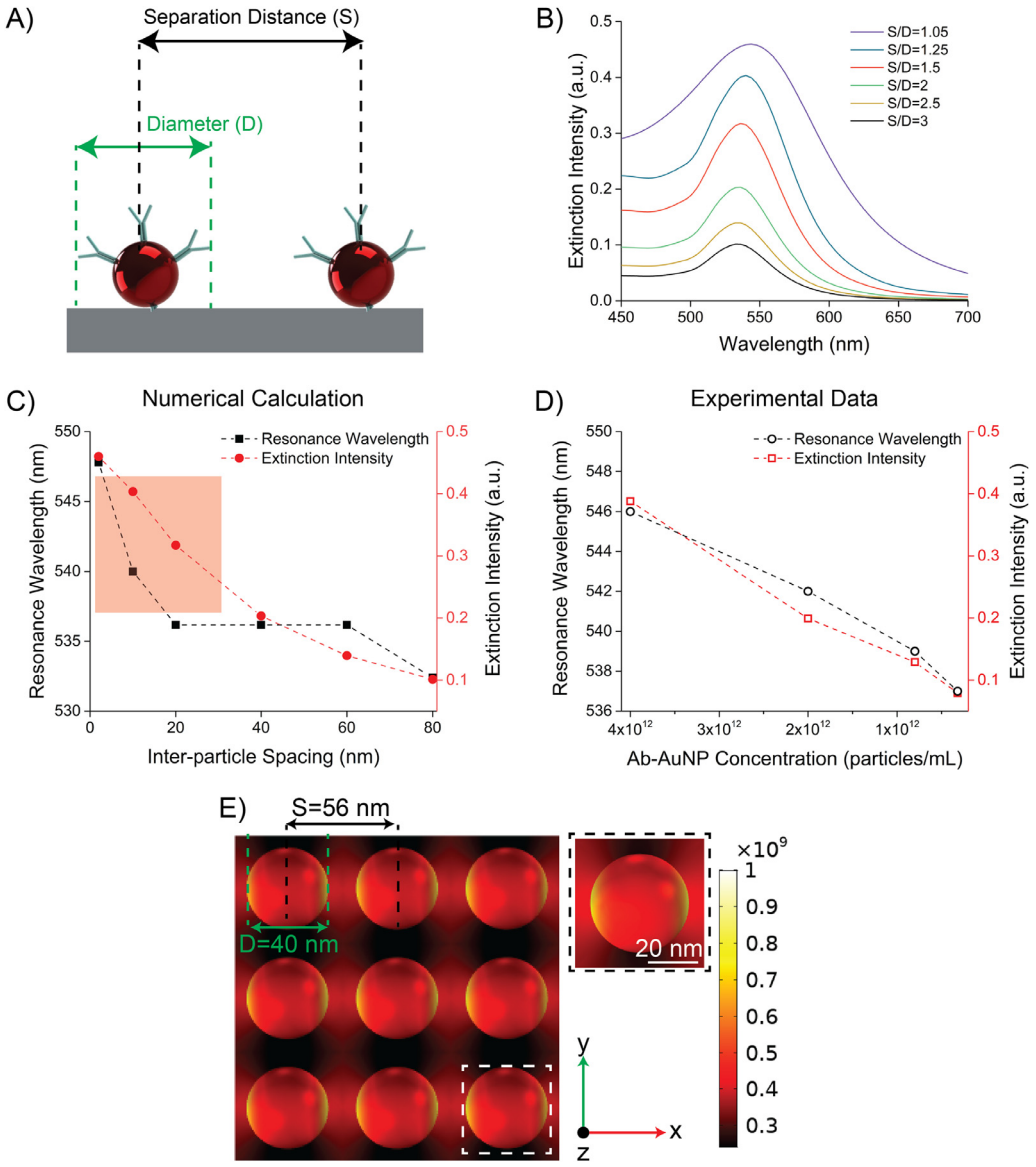


**Fig. 4.** Numerical simulations of antibody-coated gold nanoparticle (Ab-AuNP) binding on the well surface. A) Ab-AuNP with a diameter of (D) are placed on top of PLL coated polystyrene well surfaces with a separation distance (S). B) Extinction spectra for different S/D ratios are plotted. By decreasing this ratio, the extinction intensity increases and there is also a red-shift in the resonance wavelength. C) The lower inter-particle spacing results in both higher extinction intensity and red-shift in the resonance wavelength. The brown-box on the numerical calculation plot indicates that the experimental data (from 537 nm to 546 nm of resonance wavelength values) is spanning a part of the simulation space. D) High concentration of Ab-AuNP (equivalent to lower inter-particle spacing in simulations) exhibits higher extinction intensity and larger resonance wavelength red-shift. During all these experiments, the PLL concentration was 0.75 mg/mL. E) Field-distribution around the Ab-AuNPs for a $S/D = 1.4$ at resonance wavelength is presented when the lattice is illuminated with an x-polarized plane wave.

was defined as the same dilution condition with the highest HBV concentration ($10^5$ IU/mL). Peak wavelength shift caused by the control sample resulted in statistically lower signal compared to the other groups ($n$=3-6, $p$<0.05). When we applied the HBV samples, we observed the peak wavelength shifts proportional to the HBV concentrations, ranging from 1.3 ± 0.3 nm to 2.3 ± 0.3 nm.

We further designed a sandwich nanoplasmonic assay, where we applied a secondary Ab-AuNP after HBV particles were captured on the nanoplasmonic surface. We used the same Ab-AuNP (monoclonal anti-HBV HBsAg antibody-AuNP) for both the first and secondary binding layers. Before starting the assay, we defined a control experiment, which we applied the secondary Ab-AuNPs onto the first binding layer that did not have any HBV captured on the surface. We, therefore, evaluated any interactions caused by the first and the secondary Ab-AuNP binding layers in the absence of HBV capture. After creating the first binding layer, we tested the concentrations of the secondary binding layer ranging from $8 \times 10^{10}$ to $8 \times 10^{12}$ Ab-AuNPs/mL by applying to the surfaces (Fig. 5D). The interactions between the first and secondary binding layers resulted in peak wavelength shifts ranging from 0.3 nm to 0.9 nm. Since the secondary Ab-AuNP was used as an enhancement factor, we considered that the dilution rate would have two features: (i) low background not to cause non-specific signals, and (ii) sufficient number of Ab-AuNPs to bind to the captured viruses. We therefore selected $8 \times 10^{11}$ Ab-AuNPs/mL concentration of secondary binding layer for the following experiments due to the lowest non-specific interactions with the first layer in the absence of HBV on the surface, and this concentration provided enough number of Ab-AuNPs for the signal enhancement. In addition, anti-HBV HBsAg antibody-AuNP conjugates are specific for the detection of HBV. To further evaluate both non-specific interactions and specificity, there could be another option, where we could use AuNPs

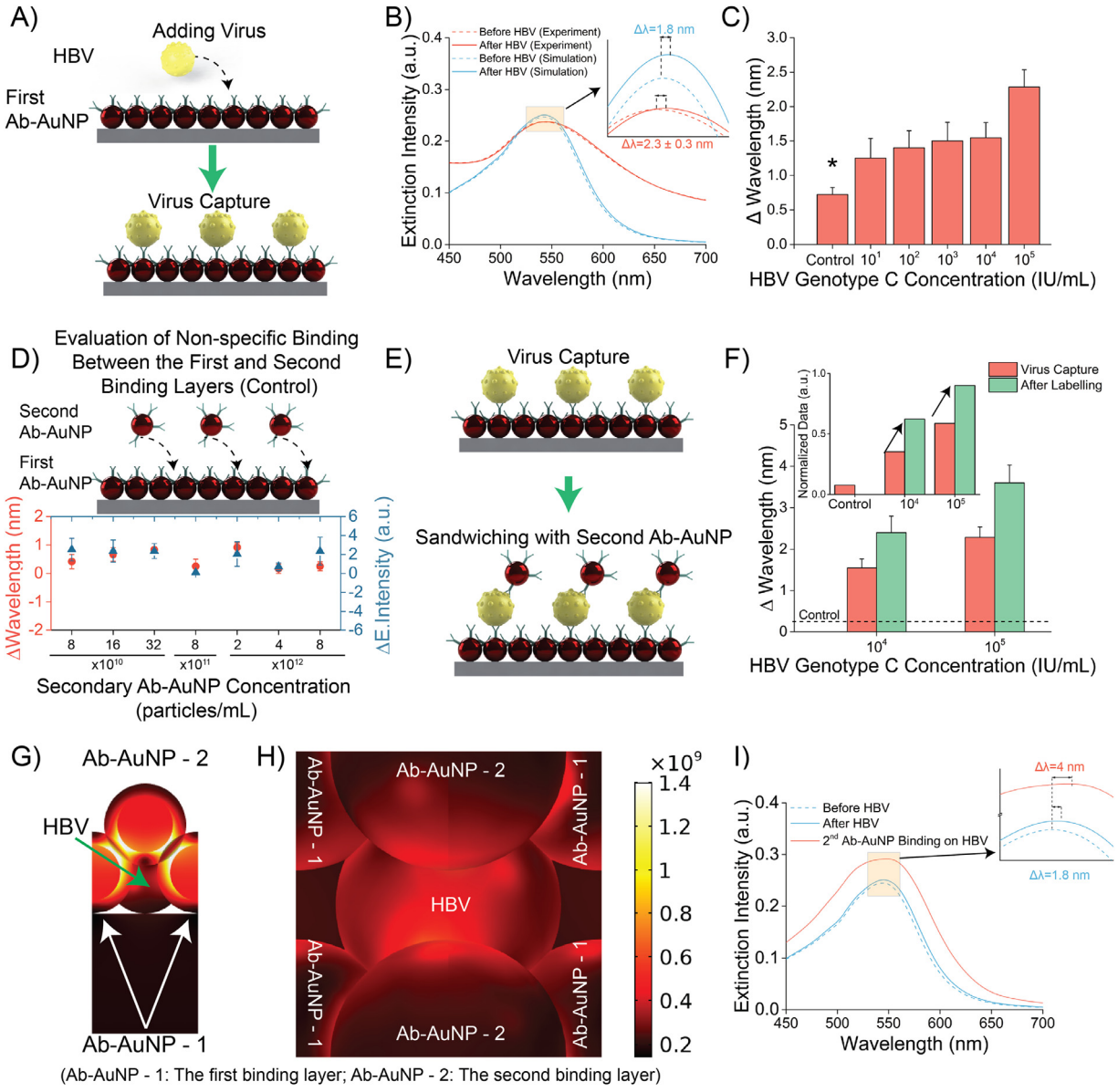


**Fig. 5.** Detection of HBV on the sensing surface. A) The well plate surface was decorated with the optimized concentrations of poly-L-lysine (PLL) and anti-HBV surface (HBs), Antigen (Ag) antibody-coated AuNP (Ab-AuNP) (monoclonal anti-HBV HBsAg antibody-AuNP). B) The extinction data recorded before (red-dashed line) and after HBV capture (red-line). The variations in the extinction spectrum were also theoretically analyzed before (blue-dashed line) and after HBV capture (blue-line). The inset represents a detailed demonstration of the wavelength shifts in both simulation and experimental data. In both cases, there is a red-shift of the resonance wavelength. In experiments, we measured a mean shift value of 2.3 ± 0.3 nm and our calculations predicted a shift of 1.8 nm. C) Further, we evaluated the platform performance with multiple HBV concentrations. As the virus stock was in serum, we used diluted serum samples as controls. HBV samples from 10 to $10^5$ IU/mL were applied onto the sensing surface and the wavelength peak data was recorded before and after virus binding. We observed that the highest concentration of HBV provided more binding contrast to the lower concentrations. The HBV stock solution was serially diluted to adjust the concentrations from 10 to $10^5$ IU/mL. Further, the control was defined as 1:1000 (v:v) dilution of serum samples in PBS in order to mimic the dilution rate when preparing the highest HBV concentration ($10^5$ IU/mL). Overall, the control sample resulted in statistically lower wavelength shifts compared to the other groups ($n$=3-6, $p$<0.05). We also observed the peak wavelength shifts proportional to the HBV concentrations. D) Before starting the sandwiching assay, we designed a control experimental set, which we applied the secondary Ab-AuNPs to the first binding layer in the absence of HBV on the surface. Here, we used the same Ab-AuNP conjugates (monoclonal anti-HBV HBsAg antibody-AuNP) for both the first and second binding layers. We therefore evaluated any interactions caused by the first and the secondary Ab-AuNP binding layers when there was no HBV captured on the surface (control). Briefly, different secondary Ab-AuNP concentrations ($8 \times 10^9$ to $8 \times 10^{11}$ Ab-AuNPs/mL) were applied after the first layer was established. The changes in wavelength peak was recorded before and after second binding layers. The signal change ranged from 0.3 to 0.9 nm of wavelength peak value, and the lowest signal was observed at $8 \times 10^{11}$ Ab-AuNPs/mL concentration. Therefore, we continued with this concentration for further experiments due to the lowest non-specific interactions with the first layer in the absence of HBV on the surface (control). E) After determining the concentration of secondary binding layer, $8 \times 10^{11}$ Ab-AuNPs/mL concentration was applied to the surface, where viruses were captured. F) Followed by the addition of secondary Ab-AuNP to the virus-bound surface, the wavelength peak values increased in different concentrations of HBV. Control data (~0.3 nm) resulted in significantly lower than that of all HBV concentrations ($n$=3-5, $p$<0.05). The inset figure presents the enhancement factors on the signal. G) Field distribution in a unit cell of the simulation space consisting of a virus at the center of the cell, four quarter primary Ab-AuNPs at the corners of the cell and two half nanospheres of secondary binding at the top. H) Top view of field distribution for the unit cell is presented. I) Calculated extinction spectra for the surface-coated with primary Ab-AuNPs (blue-dashed line), after capture of HBVs (blue-line), and after binding of secondary Ab-AuNPs (red-line). Resonance shift after the secondary Ab-AuNP binding is 4 nm which is 2.2 times larger than the shift after HBV capture. (For interpretation of the references to color in this figure legend, the reader is referred to the web version of this article.).

functionalized with a non-interacting antibody, and apply them to both or one side of the sandwich assay.

In the sandwich nanoplasmonic assay, we first applied HBV to the nanoplasmonic surfaces and incubated $8 \times 10^{11}$ Ab-AuNPs/mL for the secondary binding layer (Fig. 5E). Control (background) data was defined as the data resulted by the secondary Ab-AuNP ($8 \times 10^{11}$ Ab-AuNPs/mL concentration) when HBV was not applied (Fig. 5F). Control data (~0.3 nm) was significantly lower than that of all HBV concentrations ($n$=3-5, $p$<0.05). We evaluated two HBV concentrations ($10^4$ and $10^5$ IU/mL), caused a peak wavelength shift of 1.6 ± 0.2 nm and 2.3 ± 0.3 nm, respectively. When the secondary Ab-AuNP was applied after HBV capture, we observed additional shifts, resulting in 2.4 ± 0.4 nm for $10^4$ IU/mL and 3.6 ± 0.4 nm for $10^5$ IU/mL. We further evaluated these results by normalizing data for the control and virus concentrations ($10^4$ and $10^5$ IU/mL) before and after the secondary Ab-AuNP was applied (Fig. 5F-inset). The normalized data of control was ~0.08 a.u., which was lower than virus data (without secondary Ab-AuNP) as 0.35 a.u. for $10^4$ IU/mL and 0.59 a.u. for $10^5$ IU/mL. After applying secondary Ab-AuNP, the signals were enhanced by 1.53-1.77 times compared to the viruses captured on the surface. Our numerical simulations also support that a secondary nanoparticle binding would result to a larger resonance. Fig. 5G shows electric-field distribution at resonance for a unit cell of the structure with an Ab-AuNP in the middle of the cell, four dielectric quarter Ab-AuNPs at the corners, and two half Ab-AuNPs at the top to provide a clearer picture we plotted field distribution in a $4 \times 4$ array (Fig. 5H). Based on this simulation, the peak wavelength of extinction spectrum would shift for 4 nm when secondary Ab-AuNP bind to the surface, which is 2.2 times more than the shift observed after binding of HBVs to the primary nanoparticles. This theoretical number is larger than the experimental value as the simulations assume each gold nanoparticle on the first binding layer to have a virus and a secondary Ab-AuNP to be bound onto it.

## 3. Conclusions

In this paper, we demonstrate a dual-sensing modality of a nanoplasmonic sensor by (i) integrating Ab-AuNPs on a surface for label-free nanoplasmonic detection and (ii) sandwiching bio-targets between nanoparticles on the top and the bottom. Leveraging these two capabilities, we further (i) validated our system by measuring HBV viral loads using serum samples isolated from infected individuals, spanning a clinical relevant range from 10 to $10^5$ IU/mL, and (ii) amplified the detection signals by 1.53 – 1.77 times through a nanoplasmonic sandwiching approach. As a proof-of-concept, this unconventional approach was designed on a 96-well plate surface in a highly scalable and high-throughput. This 96-well plate format enables integration with standard lab equipment and procedures. In addition, this platform reduces assay cost and time (1 hour); presents a facile procedure (only three steps: sampling, incubation, and washing); utilizes affordable materials/reagents and standard lab tools (pipette and standard spectrometric plate reader) that potentially accelerate its accessibility to the current clinical labs without any disruptions in the workflow.

## 4. Materials and methods

### 4.1. Materials

Monoclonal anti-HBV HBsAg antibody (Gold Colloid) (Product number: 62-H05B) was purchased from Fitzgerald Industries International (North Acton, MA, USA). Poly-L-lysine (PLL) hydrobromide (Mw: 150,000-300,000 Da) (Product number: P1399) was obtained from Sigma-Aldrich (St. Louis, MO, USA). Phosphate buffered saline (PBS) (Product number: 10010-049) was purchased form Thermo Fisher Scientific (Waltham, MA, USA). Paraformaldehyde (PFA)-EM Grade (Product number: 15710) was obtained from Electron Microscopy Sciences (Hatfield, PA, USA). The 96-well plates (cellGrade™) (Product number: 781962) were purchased from the BrandTech Scientific, Inc. (Essex, CT, USA).

### 4.2. Fabrication of nanoplasmonic platform

The 96-well plate was utilized as a base substrate (polystyrene material) to create a nanoplasmonic sensor. Initially, we coated the wells by adding 100 µL of PLL hydrobromide solution diluted in PBS, spanning from 0.05 to 1 mg/mL. This solution was seeded into wells and allowed to bind for 24 hours at 4°C, creating amine-binding groups for Ab-AuNP immobilization. At the end of the incubation, PLL solution was discarded and the well surface was rinsed with PBS. Later, 50 $\mu$L of Ab-AuNP solution ranging from $8 \times 10^{10}$ to $8 \times 10^{12}$ Ab-AuNPs/mL (diluted in PBS) was applied to the PLL-coated wells and incubated at different time slots (30 min to 24 hours). After this incubation step, Ab-AuNP solution was discarded and the wells were washed once with PBS. Afterwards, the extinction intensity values of the nanoplasmonic platform were measured at the wavelength ranges from 350 to 800 nm using a standard spectrometric plate reader (Tecan Spark 10M). The optimized concentrations and incubation time were stated in the Results and Discussion section.

### 4.3. Transmission electron microscopy imaging (TEM)

The Ab-AuNPs were drop-casted on copper grids with pure carbon support film and incubated for 10 minutes. Then, the grids were washed with ultrapure water. High resolution TEM images were taken on a $C_s$ corrected FEI Titan (Thermo Fisher Scientific, USA) microscope operated at 300 kV equipped with a OneView camera (Gatan, Inc, USA).

### 4.4. Contact angle measurements

The analysis was performed using KRÜSS Drop Shape Analyzer (DSA100, Hamburg, Germany) instrument. In the measurements, we dropped a 5 µL of ultrapure water to the surface and the contact angle values were recorded. The data was reported as an average of three different drops with standard deviation values.

### 4.5. Atomic force microscope (AFM) measurements

Topographical analysis of nanoplasmonic surfaces was analyzed using an AFM instrument (Veeco MultiMode V, AS-12 “E”, California, USA) with the tapping mode. The nanoplasmonic surfaces were mounted to the AFM sample holder using double-sided carbon strip. The surfaces were imaged as 1 µm x 1 µm size.

### 4.6. FTIR-ATR spectroscopy

Bare polystyrene and nanoplasmonic surface were scanned from 500 to 3750 $cm^{-1}$ range with 2 $cm^{-1}$ of resolution using FTIR-ATR instrument (Thermo Fisher Scientific, Nicolet iS10, Waltham, MA, USA). Total light reflection was recorded for both surfaces. The data of bare polystyrene surface was subtracted the spectra of the nanoplasmonic surface to evaluate the chemical group formation.

### 4.7. Numerical simulations

RF Module of COMSOL Multiphysics is used for our electromagnetic analysis. Bloch periodic boundary conditions are applied in

two dimensions. Measurement data have been used to describe optical properties of the gold [46]. Based on previous studies on viruses, we assumed a refractive index of $n = 1.5$ in our simulations [47,48]. The structure is illuminated with a normal plane wave from the top using a periodic port with input power of $1\,W$.

### 4.8. HBV samples

The clinical samples were from a biorepository approved by the Institutional Review Board (IRB), at Beth Israel Deaconess Medical Center (BIDMC). The study conformed to the ethical guidelines of the 1975 Declaration of Helsinki. The Material Transfer Agreement (MTA) was collected between BIDMC and Stanford University. Sera were collected from patients with chronic hepatitis B prior to receiving antiviral therapy and were stored at -70°C freezer. Each sample was linked with an electronic medical record with available HBV genotype and HBV DNA titer by RT-PCR. The HBV Genotype C stock concentration was measured as $306 \times 10^6$ IU/mL. All the patient identifiers were removed prior to testing.

### 4.9. Measurements

The extinction intensity of Ab-AuNP decorated plate was measured from 350 nm to 800 nm using a standard plate reader (Tecan Spark 10M). The plasmonic data was indicated as the wavelength shift at the plasmon peak position (resonance), and all data for wavelength and extinction intensity measurements were stated as the mean of wavelength changes ± standard errors of the mean [49]. The data was rounded to the first decimal digit considering the resolution, errors, and accuracy of the position determination on the plate reader instrument.

### 4.10. HBV detection

After the nanoplasmonic surface was developed, we scanned the well surfaces (before HBV) from 350 nm to 800 nm of wavelength using a spectrometric plate reader stated above. We then applied 100 µL of HBV samples with different concentrations to the surfaces and incubated for an hour at the BSL2+ room. After the incubation, we washed the surfaces with 200 µL of PBS. The captured viruses were then fixed using 6% of paraformaldehyde (PFA) for 30 minutes, and the wells were again washed with 200 µL of PBS to remove any impurities of PFA on the surface. For measurements, we added 100 µL of PBS to each well, and scanned the surfaces again (after HBV). In the sandwich nanoplasmonic assay, after HBV capture (before PFA step), we applied the secondary Ab-AuNP ($8 \times 10^{11}$ Ab-AuNPs/mL concentration) to the well surfaces, and incubated for an hour. We then washed the surfaces with 200 µL of PBS, and followed the same procedure including the PFA fixation step, washing, and measuring as described above.

## Declaration of Competing Interests

Prof. Utkan Demirci (UD) is a founder of and has an equity interest in: (i) DxNow Inc., a company that is developing microfluidic IVF tools and imaging technologies for point-of-care diagnostic solutions, (ii) Koek Biotech, a company that is developing microfluidic technologies for clinical solutions, (iii) Levitas Inc., a company focusing on developing microfluidic products for sorting rare cells from liquid biopsy in cancer and other diseases, and (iv) Hillel Inc., a company bringing microfluidic cell phone tools to home settings. UD's interests were viewed and managed in accordance with the conflict of interest policies.

## CRediT authorship contribution statement

**Fatih Inci:** Conceptualization, Methodology, Validation, Formal analysis, Investigation, Data curation, Writing - original draft, Writing - review & editing, Visualization, Project administration. **Merve Goksin Karaaslan:** Validation, Formal analysis, Investigation, Data curation, Writing - review & editing. **Amideddin Mataji-Kojouri:** Methodology, Formal analysis, Writing - review & editing. **Pir Ahmad Shah:** Validation, Methodology, Writing - review & editing. **Yeşeren Saylan:** Formal analysis, Data curation, Writing - review & editing. **Yitian Zeng:** Methodology, Writing - review & editing. **Anirudh Avadhani:** Visualization. **Robert Sinclair:** Writing - review & editing, Supervision. **Daryl T.-Y. Lau:** Conceptualization, Methodology, Validation, Writing - original draft, Investigation, Writing - review & editing, Supervision. **Utkan Demirci:** Conceptualization, Methodology, Validation, Formal analysis, Investigation, Writing - original draft, Writing - review & editing, Supervision.

## Acknowledgments

The authors seed funding for supporting this work. We would like to thank The Scientific and Technical Research Council of Turkey (TUBITAK) for providing financial support for supporting M.G.K. (2219-International Postdoctoral research fellowship program) and Y.S. (2214A-Abroad research support for Ph.D. students) during their visit at the BAMM Labs, where this work is performed. A.M.K would like to acknowledge office of Vice-President for International Affairs from University of Tehran. A.M.K. would like to thank BAMM Lab, the Department of Radiology, Stanford University School of Medicine for his visit where this work was performed.

## Supplementary materials

Supplementary material associated with this article can be found, in the online version, at doi:10.1016/j.apmt.2020.100709.

## References

[1] K. Saha, S.S. Agasti, C. Kim, X. Li, V.M. Rotello, Gold nanoparticles in chemical and biological sensing, Chem. Rev. 112 (2012) 2739–2779, doi:10.1021/cr2001178.
[2] O. Tokel, F. Inci, U. Demirci, Advances in plasmonic technologies for point of care applications, Chem. Rev. 114 (2014) 5728–5752, doi:10.1021/cr4000623.
[3] W. Yu, W.C. Jiang, Q. Lin, T. Lu, Cavity optomechanical spring sensing of single molecules, Nat. Commun. 7 (2016) 12311, doi:10.1038/ncomms12311.
[4] A.A. Yanik, M. Huang, O. Kamohara, A. Artar, T.W. Geisbert, J.H. Connor, H. Altug, An optofluidic nanoplasmonic biosensor for direct detection of live viruses from biological media, Nano Lett. 10 (2010) 4962–4969, doi:10.1021/nl103025u.
[5] H. Inan, M. Poyraz, F. Inci, M.A. Lifson, M. Baday, B.T. Cunningham, U. Demirci, Photonic crystals: emerging biosensors and their promise for point-of-care applications, Chem. Soc. Rev. 46 (2017) 366–388, doi:10.1039/c6cs00206d.
[6] Z. Li, L. Leustean, F. Inci, M. Zheng, U. Demirci, S. Wang, Plasmonic-based platforms for diagnosis of infectious diseases at the point-of-care, Biotechnol. Adv. 37 (2019) 107440, doi:10.1016/j.biotechadv.2019.107440.
[7] Y. Zhuo, H. Hu, W. Chen, M. Lu, L. Tian, I.M. Carreira, K.D. Long, E. Chow, W.P. King, S. Singamaneni, B.T. Cunningham, Single nanoparticle detection using photonic crystal enhanced microscopy, Analyst 139 (2014) 1007–1015, doi:10.1039/c3an02295a.
[8] U.H. Yildiz, F. Inci, S. Wang, M. Toy, H.C. Tekin, A. Javaid, D.T.-Y. Lau, U. Demirci, Recent advances in micro/nanotechnologies for global control of hepatitis B infection, Biotechnol. Adv. 33 (2015) 178–190, doi:10.1016/j.biotechadv.2014.11.003.
[9] W. Asghar, M. Yuksekkaya, H. Shafiee, M. Zhang, M.O. Ozen, F. Inci, M. Kocakulak, U. Demirci, Engineering long shelf life multi-layer biologically active surfaces on microfluidic devices for point of care applications, Sci. Rep. 6 (2016) 21163, doi:10.1038/srep21163.
[10] American Cancer Society. *Can infections cause cancer?* (2016).
[11] Y. Saylan, Ö. Erdem, S. Ünal, A. Denizli, An alternative medical diagnosis method: biosensors for virus detection, Biosensors 9 (2019) 65, doi:10.3390/bios9020065.
[12] C. Fitzmaurice, C. Allen, R.M. Barber, L. Barregard, Z.A. Bhutta, H. Brenner, D.J. Dicker, O. Chimed-Orchir, R. Dandona, L. Dandona, T. Fleming,

M.H. Forouzanfar, J. Hancock, R.J. Hay, R. Hunter-Merrill, C. Huynh, H.D. Hosgood, C.O. Johnson, J.B Jonas, et al., Global, regional, and national cancer incidence, mortality, years of life lost, years lived with disability, and disability-adjusted life-years for 32 cancer groups, 1990 to 2015: a systematic analysis for the global burden of disease study global burden, JAMA Oncol. 3 (2017) 524 –548, doi:10.1001/jamaoncol.2016.5688.

[13] National Public Radio-Health. *Liver cancer is becoming a top killer in poor countries*. (2016).

[14] Institute of Medicine (US) Committee on Cancer Control in Low- and Middle-Income Countries; Editors: Frank A Sloan and Hellen Gelband. The cancer burden in low- and middle-income countries and how it is measured. (2007).

[15] K.K. Holmes, S. Bertozzi, B.R. Bloom, P. Jha, H. Gelband, L.M. DeMaria, S. Horton, Major Infectious Diseases: Key Messages from Disease Control Priorities, Third Edition. Major Infectious Diseases, (The International Bank for Reconstruction and Development / The World Bank, 2017, doi:10.1596/978-1-4648-0524-0/CH1.

[16] F. Bray, J. Ferlay, I. Soerjomataram, R.L. Siegel, L.A. Torre, A. Jemal, Global cancer statistics 2018: GLOBOCAN estimates of incidence and mortality worldwide for 36 cancers in 185 countries, CA. Cancer J. Clin. 68 (2018) 394–424, doi:10.3322/caac.21492.

[17] American Cancer Society. Key statistics about liver cancer. (2016). Available at: https://www.cancer.org/cancer/liver-cancer/about/what-is-key-statistics.html. (Accessed: 26th November 2018)

[18] M.C. Kew, Hepatocellular carcinoma in developing countries: prevention, diagnosis and treatment, World J. Hepatol. 4 (2012) 99–104, doi:10.4254/wjh.v4.i3.99.

[19] C.J. Chen, H.I. Yang, J. Su, C.L. Jen, S.L. You, S.N. Lu, G.T. Huang, U.H. Iloeje, Risk of hepatocellular carcinoma across a biological gradient of serum hepatitis B virus DNA Level, J. Am. Med. Assoc. 295 (1) (2006) 65–73, doi:10.1001/jama.295.1.65.

[20] R.W. Yucha, K.S. Hobbs, E. Hanhauser, L.E. Hogan, W. Nieves, M.O. Ozen, F. Inci, V. York, E.A. Gibson, C. Thanh, H. Shafiee, El Assal, R. Kiselinova, M. Robles, Y. P., H. Bae, K.S. Leadabrand, S. Wang, S.G. Deeks, D.R Kuritzkes, et al., High-throughput characterization of HIV-1 reservoir reactivation using a single-cell-in-droplet PCR assay, EBioMedicine 20 (2017) 217–229, doi:10.1016/j.ebiom.2017.05.006.

[21] M. Lemoine, S. Nayagam, M. Thursz, Viral hepatitis in resource-limited countries and access to antiviral therapies: current and future challenges, Future Virol. 8 (2013) 371–380, doi:10.2217/fvl.13.11.

[22] L. Stabinski, S. O'Connor, M. Barnhart, R.J. Kahn, T.E. Hamm, Prevalence of HIV and Hepatitis B virus co-infection in Sub-Saharan Africa and the potential impact and program feasibility of Hepatitis B surface antigen screening in resource-limited settings, J. Acquir. Immune Defic. Syndr. 68 (2015) S274–S285, doi:10.1097/QAI.0000000000000496.

[23] S. Chevaliez, J.M. Pawlotsky, New virological tools for screening, diagnosis and monitoring of hepatitis B and C in resource-limited settings, J. Hepatol. 69 (2018) 916–926, doi:10.1016/j.jhep.2018.05.017.

[24] C.J. Morris, M. Hill, M. de Medina, C. Herman, G.A. Cloherty, P. Martin, Comparison of detection and quantification of HBV DNA in chronic HBeAg negative and positive patients by Abbott RealTime HBV and Roche Cobas TaqMan HBV assays, J. Virol. Methods 193 (2013) 391–393, doi:10.1016/j.jviromet.2013.06.036.

[25] A.D. Chowdhury, K. Takemura, T.-C. Li, T. Suzuki, E.Y. Park, Electrical pulse-induced electrochemical biosensor for hepatitis E virus detection, Nat. Commun. 10 (2019) 3737, doi:10.1038/s41467-019-11644-5.

[26] J. Li, M.A. Baird, M.A. Davis, W. Tai, L.S. Zweifel, K.M.A. Waldorf, M. Gale, L. Rajagopal, R.H. Pierce, X. Gao, Dramatic enhancement of the detection limits of bioassays via ultrafast deposition of polydopamine, Nat. Biomed. Eng. 1 (2017) 0082, doi:10.1038/s41551-017-0082.

[27] J. Chi, B. Gao, M. Sun, F. Zhang, E. Su, H. Liu, Z. Gu, Patterned photonic nitrocellulose for pseudopaper ELISA, Anal. Chem. 89 (2017) 7727–7733, doi:10.1021/acs.analchem.7b01732.

[28] O. Tokel, U.H. Yildiz, F. Inci, N.G. Durmus, O.O. Ekiz, B. Turker, C. Cetin, S. Rao, K. Sridhar, N. Natarajan, H. Shafiee, A. Dana, U. Demirci, Portable microfluidic integrated plasmonic platform for pathogen detection, Sci. Rep. 5 (2015) 9152, doi:10.1038/srep09152.

[29] F. Inci, C. Filippini, M. Baday, M.O. Ozen, S. Calamak, N.G. Durmus, S. Wang, E. Hanhauser, K.S. Hobbs, F. Juillard, P.P. Kuang, M.L. Vetter, M. Carocci, H.S. Yamamoto, Y. Takagi, U.H. Yildiz, D. Akin, D.R. Wesemann, A Singhal, et al., Multitarget, quantitative nanoplasmonic electrical field-enhanced resonating device (NE $^2$ RD) for diagnostics, Proc. Natl. Acad. Sci. 112 (2015) E4354–E4363, doi:10.1073/pnas.1510824112.

[30] F. Inci, O. Tokel, S. Wang, U.A. Gurkan, S. Tasoglu, D.R. Kuritzkes, U. Demirci, Nanoplasmonic quantitative detection of intact viruses from unprocessed whole blood, ACS Nano 7 (2013) 4733–4745, doi:10.1021/nn3036232.

[31] F. Inci, U. Celik, B. Turken, H.Ö. Özer, F.N. Kok, Construction of P-glycoprotein incorporated tethered lipid bilayer membranes, Biochem. Biophys. Rep. 2 (2015) 115–122, doi:10.1016/j.bbrep.2015.05.012.

[32] C.Y. Chang, H.T. Lin, M.S. Lai, T.Y. Shieh, C.C. Peng, M.H. Shih, Y.C. Tung, Flexible localized surface plasmon resonance sensor with metal–insulator–metal nanodisks on PDMS substrate, Sci. Rep. 8 (2018) 11812, doi:10.1038/s41598-018-30180-8.

[33] Y. Shen, J. Zhou, T. Liu, Y. Tao, R. Jiang, M. Liu, G. Xiao, J. Zhu, Z.K. Zhou, X. Wang, C. Jin, J. Wang, Plasmonic gold mushroom arrays with refractive index sensing figures of merit approaching the theoretical limit, Nat. Commun. 4 (2013) 2381, doi:10.1038/ncomms3381.

[34] F. Yesilkoy, R.A. Terborg, J. Pello, A.A. Belushkin, Y. Jahani, V. Pruneri, H. Altug, Phase-sensitive plasmonic biosensor using a portable and large field-of-view interferometric microarray imager, Light Sci. Appl. 7 (2018) 17152, doi:10.1038/lsa.2017.152.

[35] G.A. Lopez, M.C. Estevez, M. Soler, L.M. Lechuga, Recent advances in nanoplasmonic biosensors: applications and lab-on-a-chip integration, Nanophotonics 6 (2017) 123–136, doi:10.1515/nanoph-2016-0101.

[36] M.A. Lifson, M.O. Ozen, F. Inci, S.Q. Wang, H. Inan, M. Baday, T.J. Henrich, U. Demirci, Advances in biosensing strategies for HIV-1 detection, diagnosis, and therapeutic monitoring, Adv. Drug. Deliv. Rev. 103 (2016) 90–104, doi:10.1016/j.addr.2016.05.018.

[37] S. Tasoglu, C. Tekin, F. Inci, F. Knowlton, S. Wang, S. Q., F. Wang-Johanning, G. Johanning, D. Colevas, U. Demirci, Advances in nanotechnology and microfluidics for human papillomavirus diagnostics, Proc. IEEE 103 (2015) 161–178, doi:10.1109/JPROC.2014.2384836.

[38] Y. Saylan, A. Denizli, Molecular fingerprints of hemoglobin on a nanofilm chip, Sensors 18 (2018) 3016, doi:10.3390/s18093016.

[39] C.D. Chin, T. Laksanasopin, Y.K. Cheung, D. Steinmiller, V. Linder, H. Parsa, J. Wang, H. Moore, R. Rouse, G. Umviligihozo, E. Karita, L. Mwambarangwe, S.L. Braunstein, J. Van De Wijgert, R. Sahabo, J.E. Justman, W. El-Sadr, S.K. Sia, Microfluidics-based diagnostics of infectious diseases in the developing world, Nat. Med. 17 (2011) 1015, doi:10.1038/nm.2408.

[40] H. Im, H. Shao, Y.I. Park, V.M. Peterson, C.M. Castro, R. Weissleder, H. Lee, Label-free detection and molecular profiling of exosomes with a nanoplasmonic sensor, Nat. Biotechnol. 32 (2014) 490–495, doi:10.1038/nbt.2886.

[41] K. Lee, K. Fraser, B. Ghaddar, K. Yang, E. Kim, L. Balaj, E.A. Chiocca, X.O. Breakefield, H. Lee, R. Weissleder, Multiplexed profiling of single extracellular vesicles, ACS Nano 12 (2018) 494–503, doi:10.1021/acsnano.7b07060.

[42] C.S. Kosack, A.L. Page, P.R. Klatser, A guide to aid the selection of diagnostic tests, Bull. World Health Organ. 95 (2017) 639–645, doi:10.2471/BLT.16.187468.

[43] P.K. Drain, E.P. Hyle, F. Noubary, K.A. Freedberg, D. Wilson, W.R. Bishai, W. Rodriguez, I.V. Bassett, Diagnostic point-of-care tests in resource-limited settings, Lancet Infect. Dis. 14 (2014) 239–249, doi:10.1016/S1473-3099(13)70250-0.

[44] T. Sainsbury, T. Ikuno, D. Okawa, D. Pacilé, J.M.J. Fréchet, A. Zettl, Self-assembly of gold nanoparticles at the surface of amine- and thiol-functionalized boron nitride nanotubes, J. Phys. Chem. C 111 (2007) 12992–12999, doi:10.1021/jp072958n.

[45] N.A. Terrault, A.S.F. Lok, B.J. McMahon, K.M. Chang, J.P. Hwang, M.M. Jonas, R.S. Brown, N.H. Bzowej, J.B. Wong, Update on prevention, diagnosis, and treatment of chronic hepatitis B: AASLD 2018 hepatitis B guidance, Hepatology 67 (2018) 1560–1599, doi:10.1002/hep.29800.

[46] P.B. Johnson, R.W. Christy, Optical constants of the noble metals, Phys. Rev. B 6 (1972) 4370–4379, doi:10.1103/PhysRevB.6.4370.

[47] O. Block, A. Mitra, L. Novotny, C. Dykes, A rapid label-free method for quantitation of human immunodeficiency virus type-1 particles by nanospectroscopy, J. Virol. Methods 182 (2012) 70–75, doi:10.1016/j.jviromet.2012.03.012.

[48] M. Boccara, Y. Fedala, C.V. Bryan, M. Bailly-, C. Bowler, &, A.C. Boccara, Counting and differentiating aquatic biotic nanoparticles by full-field interferometry : from laboratory tests to Tara Oceans sample analysis, Biomed. Opt. Express 7 (2016) 3736–3746, doi:10.1364/BOE.7.003736.

[49] J.R. Taylor, An introduction to error analysis: the study of uncertainties in physical measurements, Phys. Today 51 (1998) 57–58, doi:10.1063/1.882103.